$K^{*+}Y_{gs}$ photoproduction at the BGOOD experiment

Martin Ludwig

Bachelorarbeit in Physik
angefertigt im Physikalischen Institut

vorgelegt der
Mathematisch-Naturwissenschaftlichen Fakultät
der
Rheinischen Friedrich-Wilhelms-Universität
Bonn

April 2024

Ich versichere, dass ich diese Arbeit selbstständig verfasst und keine anderen als die angegebenen Quellen und Hilfsmittel benutzt sowie die Zitate kenntlich gemacht habe.

Bonn, ...
                Datum   Unterschrift

1. Gutachter: Prof. Dr. Hartmut Schmieden
2. Gutachter: Dr. Thomas Jude

Acknowledgements

Contents

v

Introduction

In recent years, a variety of exotic hadrons, comprising more valence quarks than conventional mesons ($q\bar{q}$) and baryons (qqq), have been discovered. Among these multiquark states are the XYZ mesons and the P_c pentaquarks, all of which have in common that they contain heavy charm quarks [1]. This naturally raises the question of whether such exotic structures are also realized in the light quark sector.

Indeed, evidence has been found suggesting that this is the case: In measurements of the $\gamma p \rightarrow K^0\Sigma^+$ and $\gamma p \rightarrow K^+\Sigma^0$ differential cross sections [2, 3], unexpected structures have been observed. In the proximity of certain thresholds, the differential cross section at forward angles seems to suddenly drop, possibly caused by a dynamically generated resonance that drives these channels until there is enough energy for producing the particles involved in this resonance freely. The amount of reaction strength that gets lost in these channels should then appear in other channels.

The aim of this work is to investigate the $\gamma p \rightarrow K^{*+}Y_{\mathrm{gs}}$ photoproduction channel, where Y_{gs} stands for a ground-state hyperon. which in this case could be the Λ or the Σ^0. It is to be examined whether and how these channels can be identified with the BGOOD experiment, thus laying the foundation for a possible later determination of the cross sections of these reactions. The BGOOD experiment at ELSA is ideal for studying these reactions as it combines a central calorimeter for neutral meson reconstruction with a forward spectrometer that allows for charged particle identification up to very forward angles.

This thesis is organized as follows: Chapter 2 briefly introduces the Standard Model and provides a concise overview of exotic hadrons. In this context, the motivation for investigating the given reaction channel is also discussed in more detail. Chapter 3 explains the experimental setup of BGOOD, while Chapter 4 illustrates how the data analysis in principle works and lists some properties of the emerging particles. In Chapter 5, the actual particle reconstruction is performed step by step. Chapter 6 then provides an outlook on how to determine a cross section based on the results of this thesis before finally, in Chapter 7, the results are discussed and summarized.

Physical Context

2.1 The Standard Model

The Standard Model of particle physics is the best model that physicists currently have to explain the structure of matter. It describes all known elementary particles and how they interact with each other. The Standard Model is a quantum field theory, where every elementary particle is understood as an excitation of its underlying field.

One distinguishes between elementary fermions with half-integer spin (quarks and leptons) and elementary bosons with integer spin (gauge and scalar bosons). Starting with the fermions, there are three generations of quarks and their corresponding antiquarks, as well as three generations of leptons and antileptons (see figure 2.1). The generations differ by their particle masses: Up, down, and strange quarks are referred to as the "light" quark sector, whereas charm, bottom, and top quarks are in the "heavy" quark sector.

While quarks bear electrical charge and can therefore interact electromagnetically, they stand out due to also having color charge: A quark is either red, green, or blue, and an antiquark is either antired, antigreen, or antiblue. Quarks with different color charges are bound together by the strong interaction. This process can be described by the exchange of gluons, through which quarks can change their colors.

In nature, only color-neutral particles are observed. This can be achieved by a combination of three quarks with different colors (analogous to additive color mixing, red, green, and blue yield white), called a baryon, or by a combination of a quark and an antiquark with opposite colors, called a meson.

2.2 Exotic Hadrons

Since the introduction of the quark model in the 1960s, most physicists believed that qqq baryons and $q\bar{q}$ mesons are the only bound states of quarks, although more complex states, so-called "exotic" hadrons, are not in principle forbidden by quantum chromodynamcis. However, since the beginning of the millennium, experiments started reporting unexpected resonances that did not fit into the conventional quark model anymore.

Among these resonances there is the $X(3872)$ particle which was first found by the Belle experiment in 2003 [5] and was later confirmed by other experiments such as BaBar [6] and LHCb [7]. It is now considered to be a $c\bar{c}u\bar{u}$ tetraquark state, possibly made up by a molecular-like binding of a D^0 meson and
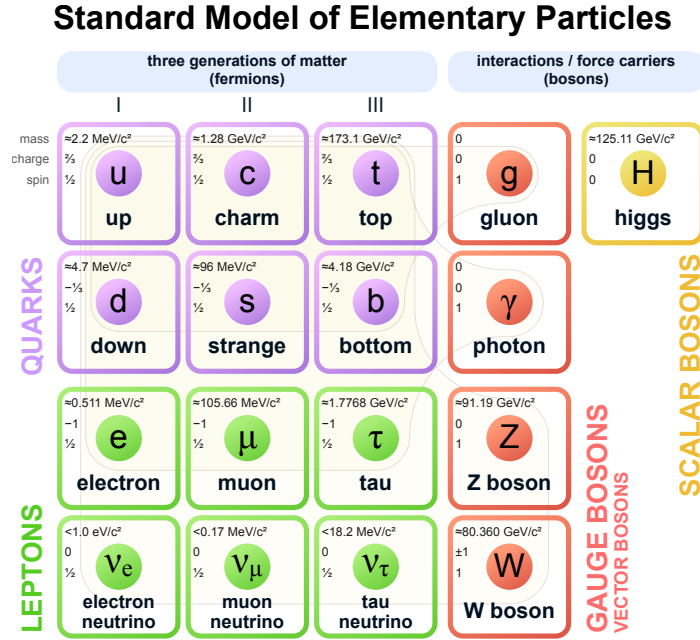
Standard Model of Elementary Particles

Figure 2.1: Elementary particles of the Standard Model. The brown loops indicate which gauge bosons couple to which fermions. For each of the fermions, there exists a corresponding antiparticle, which is not depicted in the illustration. Figure taken from [4].

a $\bar{D}^{*0}$ meson [1]. This assumption is supported by the fact that the $X(3872)$ is right at the open-charm[1] $D^0\bar{D}^{*0}$ threshold. In recent years, a variety of other possible tetraquark states called XYZ mesons have been observed [1].

In 2015, LHCb announced the observation of the pentaquark states $P_c^+(4380)$ and $P_c^+(4450)$ showing up in the bottom Lambda decay $\Lambda_b^0 \rightarrow J/\psi K^- p$ [8]. In a later publication [9], the $P_c^+(4450)$ was revealed as being the average of the two states $P_c^+(4440)$ and $P_c^+(4457)$. Additionally, another state was observed, called the $P_c^+(4312)$. Like for the $X(3872)$, the exact binding mechanism of the quarks inside these states is still unknown but their proximity to several $D^{(*)}\Sigma_c^{(*)}$ thresholds indicates they may be a molecular-like bound state of $D^{(*)}\Sigma_c^{(*)}$.

While the above-mentioned particles contain heavy charm-quarks, there are also hints for exotic hadrons in the light quark sector: In 2012, the CBELSA/TAPS collaboration reported on an anomaly in the $\gamma p \rightarrow K^0\Sigma^+$ cross section [2]. They observed a peak in the total cross section at around $W = 1\,900\,\mathrm{MeV}$, followed by a downfall at $W = 2\,000\,\mathrm{MeV}$, right between the $K^{*+}\Lambda$ and the $K^{*0}\Sigma^+$ thresholds. This downfall especially sticks out in the differential cross section for forward-directed K^0, as can be seen in Figure 2.2. Moreover, the differential cross section becomes increasingly forward-peaked with higher energies before it suddenly returns to a flat distribution beyond the K^* threshold. Partial wave analysis models of kaon photoproduction like K-MAID [10] and SAID [11] failed to reproduce the experimental observations. However, a model by Ramos and Oset [12] provides a possible explanation of

---

[1] If a particle has no net charm, i.e. it contains as many charm quarks as anti-charm quarks, one speaks of "hidden" charm. This is, for example, the case for the $X(3872)$ particle. If, on the other hand, a particle has a non-vanishing net charm, like the D meson, one speaks of "open" charm.
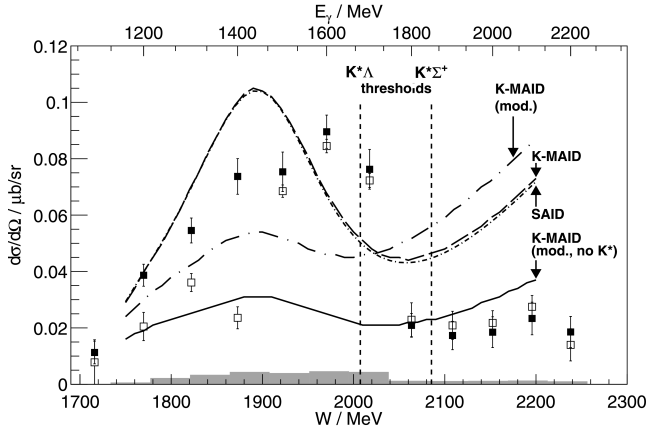
3

Figure 2.2: Differential cross section for $\gamma p \rightarrow K^0\Sigma^+$ as a function of center-of-mass energy W (black squares) for $0.6 < \cos\theta_{CM}^K < 1.0$. The grey bars on the abscissa are estimates of the systematic uncertainties. Between the $K^{*+}\Lambda$ and the $K^{*0}\Sigma+$ thresholds, the cross section suddenly drops. The SAID and K-MAID partial wave analysis models (solid and dashed lines) fail to reproduce the experimental data. Figure taken from [2].

the observed features by a vector meson-baryon dynamically generated state, the $N^*(2030)$. Assuming the P_c pentaquarks are indeed molecular-like $D^{(*)}\Sigma_c^{(*)}$ states, by replacing the charm quarks by strange quarks, potential light pentaquarks should be $K^{(*)}\Sigma^{(*)}$ bound states. Indeed, the proposed $N^*(2030)$ is close to the $K^{*+}\Sigma^0$ threshold. The same model by Ramos and Oset also predicts a peak in the $\gamma n \rightarrow K^0\Sigma^0$ cross section and indeed, the investigation of this channel at the BGOOD experiment [13] is consistent with the existence of this peak. However, statistics are relatively poor and further data is necessary to confirm this observation.

Another possible indication for exotic structures in the light quark sector appeared in the measurement of the $\gamma p \rightarrow K^+\Sigma^0$ differential cross section at BGOOD [3]. Namely, a cusp-like structure shows up at about $W = 1\,900\,\text{MeV}$, which becomes more distinct at most forward angles ($\cos\theta_{CM}^K > 0.98$), where the differential cross section suddenly drops to half of its value (see Figure 2.3). An extrapolation of the data to minimum momentum transfer $t_{\min}$ and thus $\cos\theta_{CM}^K = 1$ even shows a reduction of 75 %. This may be interpreted as an off-shell contribution becoming on-shell.

The thresholds for $K^{*+}\Lambda$ and $K^{*+}\Sigma^0$ are $W = 2\,007\,\text{MeV}$ and $W = 2\,084\,\text{MeV}$, respectively. They therefore fall in the energy region where unexpected structures in the above-mentioned channels appear. An investigation of $\gamma p \rightarrow K^{*+}Y_{gs}$ photoproduction could therefore provide hints for what causes these structures.
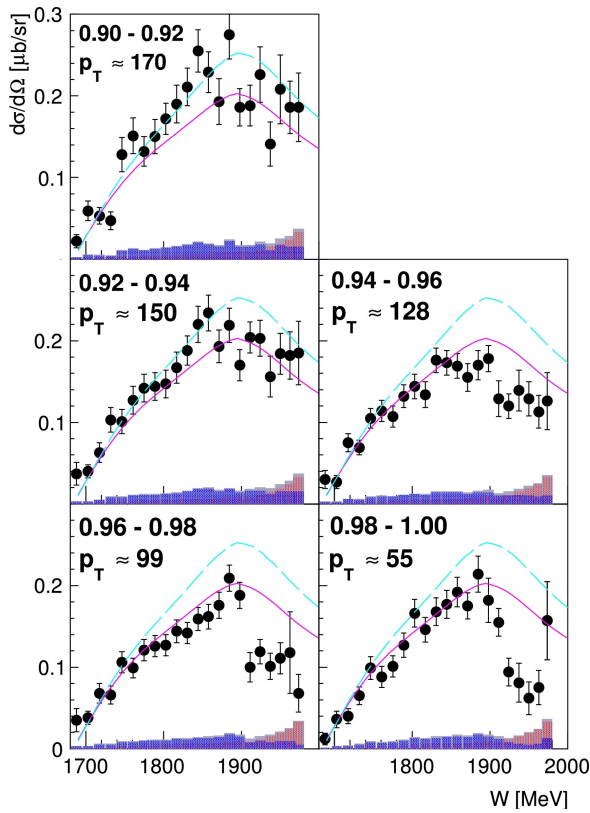
4

Figure 2.3: Differential cross section for $\gamma p \rightarrow K^+\Sigma^0$ as a function of center-of-mass energy W (black circles) for various intervals of $\cos\theta_{CM}^K$, labelled at the top left. The bars on the abscissa state the systematic uncertainties, divided into scaling, fitting and summed uncertainties (blue, red and grey, respectively). A downfall at $W =$ 1 900 MeV can be seen, which becomes particularly prominent at most forward angles. The magenta and cyan lines are results from the Bonn-Gatchina partial wave analysis model [14], which does not reproduce the cusp properly. Figure taken from [3].

Experimental Setup

The BGOOD experiment [15] is located at the Physikalisches Institut of the University of Bonn, and alongside Crystal Barrel, it is one of two photoproduction experiments at the electron accelerator ELSA. Photoproduction requires converting the electron beam of ELSA into a photon beam through bremsstrahlung, which then interacts with a fixed proton target (liquid hydrogen). This process results in the production of hadrons, and their observation, or the observation of their decay products, is performed using the various detectors of the experiment. An overview of the experiment and its components can be seen in Figure 3.1. Its name "BGOOD" is derived from the central **BGO** calorimeter and the **O**pen **D**ipole magnet, which deflects forward-going charged particles, allowing for the determination of their momenta.
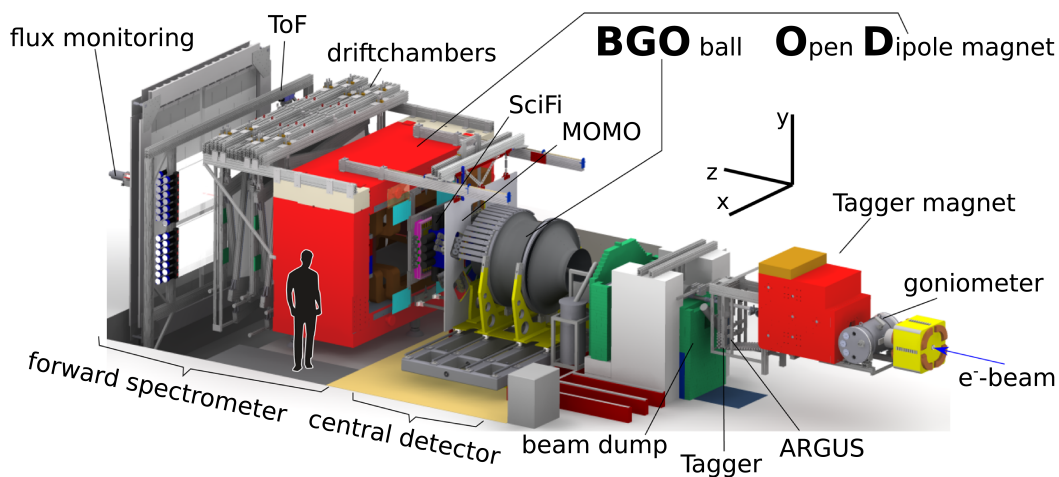

Figure 3.1: Overview of the BGOOD experiment. Figure taken from [15].

3.1 ELSA

The information presented in this subsection is taken from [16]. "ELSA" stands for **EL**ectron **S**tretcher **A**ccelerator and consists of three parts, as shown in Figure 3.2. First, electrons are produced by

thermionic emission and are accelerated by a linear accelerator (LINAC2) up to an energy of 26 MeV. Subsequently, the electrons are inserted into the booster synchrotron, which has a circumference of 69.9 m and accelerates them to energies between 0.5 GeV and 1.6 GeV. Finally, bunches of electrons are injected into the 164.4 m circumference stretcher ring, where maximum energies of 3.2 GeV can be reached. As depicted in Figure 3.2, dipole magnets bend the electrons, and quadrupole magnets are used to focus the beam horizontally and vertically. The acceleration occurs in the radio frequency cavities at a frequency of 500 MHz, resulting in electron bunches separated by 2 ns. This quasi-continuous beam is extracted by extraction magnets and directed towards the experiment.
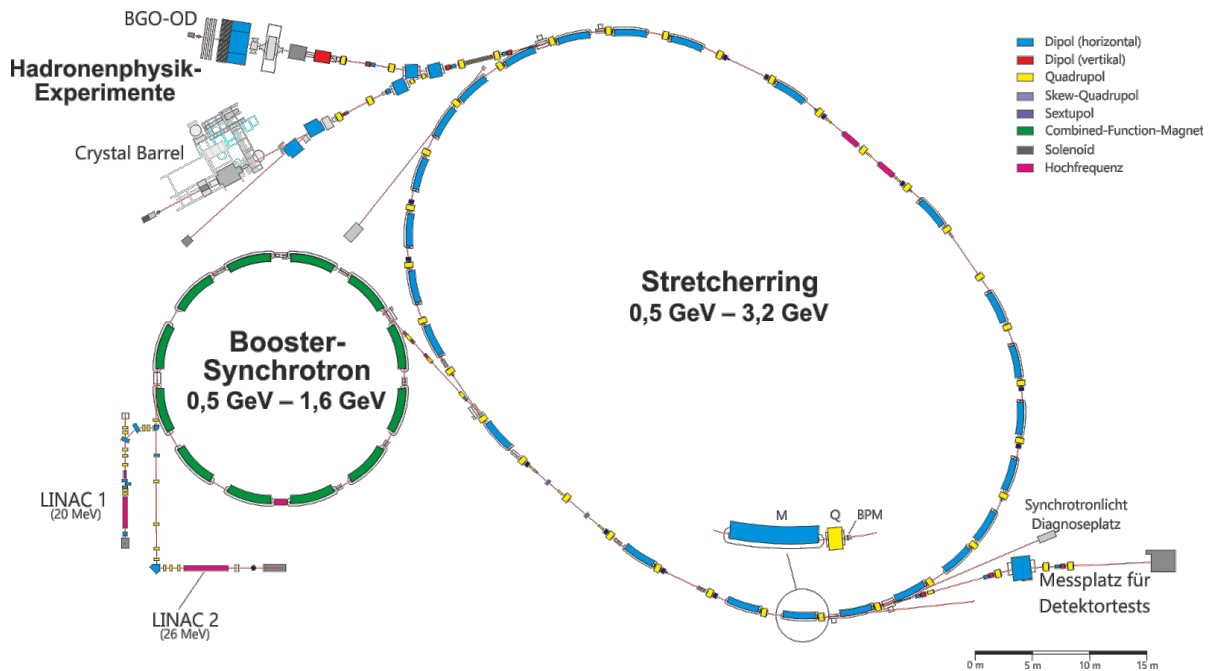

Figure 3.2: Overview of the ELSA accelerator facility. Figure taken from [16].

3.2 Photon Tagging System

The photon tagger's role is to generate a photon beam with a known energy. To achieve this, the ELSA electron beam hits a thin radiator, producing a bremsstrahlung photon beam. The post-bremsstrahlung electrons are deflected by the tagger magnet and detected in the tagger hodoscope, a detector made up of 120 overlapping plastic scintillators. By measuring the position of the incident electron, its energy is determined. The difference between the energy of the incoming electron beam and the energy measured in the hodoscope yields the energy of the photon beam (see Figure 3.3). The geometry of the tagger hodoscope allows tagging photons with energies between 10 % and 90 % of the energy E_0 of the incident electron beam, resulting in a maximum photon energy of $E_\gamma \approx 2\,880$ MeV. The deflected electrons are stopped in the beam dump, whereas the photons continue to the central detector, where they interact with the proton target.
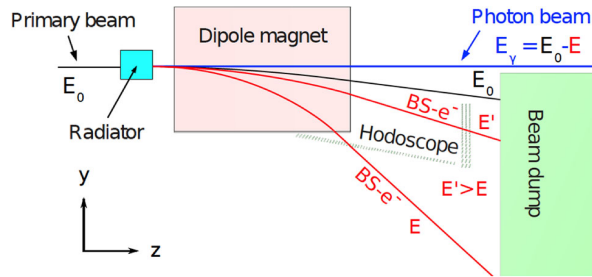
Figure 3.3: Side view and functionality of the photon tagger. Figure taken from [15].

3.3 Central Detector

The central detector (see Figure 3.4) encompasses the target, which is an aluminum cylinder filled with liquid hydrogen or deuterium at a temperature of around 20 K. Two target cells, with lengths of 6 cm and 12 cm, are available. The target cell is directly surrounded by two coaxial cylindrical multi-wire proportional chambers (MWPC). While these detectors allow for precise measurements of charged particle tracks, they were not used for this thesis as they were not operational during data taking. The MWPC is, in turn, surrounded by the scintillator barrel, which has very high detection efficiency for charged particles and a low efficiency for uncharged particles. It enables the determination of whether a hit in the BGO was caused by a charged or a neutral particle.

Finally, particles are stopped in the BGO calorimeter, where their energy is determined. The calorimeter consists of 480 scintillating crystals made of bismuth germanium oxide $(\mathrm{Bi_4GeO_4})_3$ (abbreviated as BGO) and due to its shape, it is commonly referred to as the BGO "Rugby Ball". The crystals cover the full azimuthal angle range and a polar angle range from 25° to 155°. They are optimized for the detection of photons that produce e^+e^- pairs within them, leading to subsequent electromagnetic showers. The scintillation light produced as a result is captured by photomultipliers and is proportional to the deposited energy.

Two further intermediate detectors cover the polar angle range between the central detector and the forward spectrometer (10° to 25°): A scintillator ring (SciRi) containing 96 plastic scintillators and a multi-gap resistive plate chamber (MRPC), which is still under construction. Both are not used in this thesis.

3.4 Forward Spectrometer

The forward spectrometer monitors particles with polar angles from 12° up to 1.5° and utilizes a large open dipole magnet to bend the trajectories of charged particles. The latter are measured before and after the magnet to determine their momentum from the curvature.

The tracking before the magnet is handled by two scintillating fiber detectors, MOMO and SciFi. In MOMO, 672 scintillating fibers with a diameter of 2.5 mm are arranged in six trapezoidal modules, rotated by 60° against each other. SciFi consists of 640 scintillating fibers with a diameter of 3 mm, with one half of them aligned in a horizontal layer and the other half in a vertical layer. Both detectors have a hole in their center, allowing photons that did not interact with the target to pass through without producing a signal. Moreover, the photomultipliers of both detectors are magnetically shielded to prevent the fringe magnetic field from the open dipole magnet from affecting their performance by distorting the
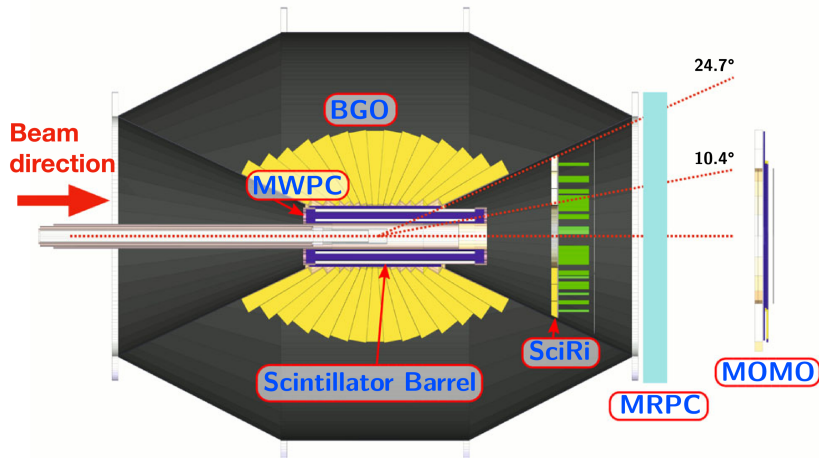
Figure 3.4: Cross-sectional view of the central detector system. The target in the center is surrounded by the cylindrical MWPC, the scintillator barrel and the BGO crystals. Figure taken from [15].

trajectories of the photoelectrons.

Behind the magnet, the particle tracks are measured by eight double-layer drift chambers and three time-of-flight (ToF) walls. The drift chambers are oriented in four different ways: horizontally, vertically, and tilted by $9°$ against the vertical in each direction. They have a sensitive area of $246 \times 123 \, \text{cm}^2$. Their central region has been made insensitive so that the intense photon beam does not cause signal overflow or even damage to the chambers.

The drift chambers are complemented by the ToF walls located behind them, at a distance of $5.6 \, \text{m}$ from the target. They extend over a total area of $3 \times 3 \, \text{m}^2$ with a gap in the center to allow the photon beam and produced e^+e^- pairs to pass through. The ToF walls have good time resolution and deliver the stop signal for the time measurement that has been started at the tagger. Thereby, the particle β can be determined, and, together with the momentum value, its mass can be calculated.

3.5 Flux Monitoring

Finally, situated more than $7 \, \text{m}$ away from the target behind the forward spectrometer, the photon flux monitoring system is placed. Two detectors, the gamma intensity monitor (GIM) and the flux monitor (FluMo), are used to measure how many photons pass through the experiment, as this flux factor is needed for cross section determination.

GIM is made of lead glass and is very sensitive, as it fully absorbs the beam photons. Within the lead glass, these photons produce electromagnetic showers, which are detected by the generated Cherenkov light. GIM is only used for calibration purposes at low beam energies.

Actual flux measurements during data collection are carried out by FluMo. It consists of five plastic scintillators in a row detecting e^+e^- pairs produced by the photons. Compared to the GIM, only a small fraction of the flux is measured, but through calibration with GIM, its detection efficiency, and hence the full photon flux, can be calculated.

3.6 Trigger and Data Acquisition

Data from the detectors are not stored permanently, as that would result in a vast amount of useless data, for example, from noise in the detectors. Instead, several local triggers are implemented to ensure that a particle has actually hit a detector or a certain energy sum has been deposited. This is accomplished by discriminators that are connected to the photomultipliers and output a digital signal only after a certain voltage threshold is reached. In the global trigger, signals from local triggers are combined via logic gates to finally decide whether to save or discard data. There are various trigger conditions possible, differing in how restrictive they are, resulting in varying output rates. After triggering, the data acquisition system reads out the raw data and combines data from the different detectors into one event, which is then stored on disk.

Analysis Procedure

4.1 Data Processing

Immediately after data acquisition with the BGOOD experiment, initially only raw data in the form of voltage signals from individual detectors are available. In a pre-analysis, these data must first be decoded and calibrated using a calibration database. Moreover, hits in single detector channels are examined for spatial and temporal coincidences and, if applicable, combined into clusters. Finally, clusters from several detectors originating from the same particle are incorporated into a track (for details, see [17]).

This pre-analysis is performed by ExPlORA[1], a framework originally developed by the CBELSA/TAPS collaboration for the Crystal Barrel experiment. It is an extension to the C++ framework ROOT [18], which is the standard framework used in particle physics analysis. In principle, it is possible to do the entire analysis with ExPlORA. However, as this is relatively slow and requires to write a plugin for each analysis step, the ExPlORA data was exported as a set of Lorentz vectors and further analysis was done with ROOT.

4.2 Data Simulation

It is extremely useful and, at the latest for the determination of the reconstruction efficiency (see section 6.2) even necessary to work with simulated data. The simulation of this data is based on Monte Carlo methods and is implemented in the ExPlORA framework too.

As a first step of the simulation, it is deduced which particles occur in the initial and final states given a certain reaction channel and target. The energy of the incident photon is randomly generated and follows the distribution of the bremsstrahlung spectrum. The generation of the momentum and direction of particles in the final state can be done in two ways: For known reactions, their differential cross-section can be used. However, in most practical applications, this is unknown, and the phase space must be considered. That is, as energy and momentum conservation put restrictions on the kinematics of a particle reaction, specific final states have varying probabilities given a known initial state. Based on this probability distribution, the final state four-momenta are determined randomly. Further information about the event generator can be found in [19].

---

[1] **Ex**tended **Pl**uggable **O**bjectoriented **R**OOTified **A**nalysis

After that, the GEANT4 toolkit [20] is used to simulate the passage of the final state particles and their decay products through the detectors. This determines whether a particle is detected and, if so, where and with what energy. The outcome of the simulation is a data set that can be analyzed in the same way as real data.

4.3 Four-vector Calculations

Mathematically, the analysis is based on the four-vector formalism, which naturally incorporates special relativity. The scalar product of two four-vectors is invariant under Lorentz transformations. For example, the square of a four-momentum vector $p = (E, \mathbf{p})$ yields, according to the relativistic energy-momentum relation, the invariant mass:

$$p^2 = p^\mu p_\mu = E^2 - \mathbf{p}^2 = m^2 \qquad \text{(natural units: } c = 1\text{)}$$

In the analysis, four-momentum conservation is used to reconstruct particles. In principle, two cases can occur:

1. All four-momenta of the final state are known. Then, they can be added and their invariant mass can be calculated to obtain intermediate particles. This is, for example, done to reconstruct the π^0 from its $\pi^0 \to \gamma\gamma$ decay (see section 5.3), where the two photons are detected in the BGO ball.

2. All four-momenta of the initial and the final state are known except for one. In this case, the missing four-momentum is also determinate by four-momentum conservation and the so called "missing mass" to this particle can be calculated. This technique is, for instance, used to reconstruct the Λ/Σ^0 in the investigated $\gamma p \to K^{*+} Y_{\text{gs}}$ channel.

4.4 Properties of the Emerging Particles

In photoproduction off the proton at the BGOOD experiment, center-of-mass energies up to $W \approx 2\,500\,\text{MeV}$ can be reached. That is enough to produce strange quarks but not enough to produce heavier flavors. Therefore, the hadrons emerging in the experiment can be found in the $SU(3)_{\text{flavor}}$ multiplets depicted in Figure 4.1 and 4.2. These multiplets can be constructed group theoretically and originate from the fact that the Hamiltonian for a system of up, down, and strange quarks is almost flavor symmetric, as the strong interaction treats all quark flavors equally and the difference in these quark masses is relatively small compared to the binding energy of hadrons[2].

4.4.1 Mesons

The two meson multiplets are displayed in Figure 4.1. They are plotted in terms of the flavor quantum numbers I_3 and S, where the isospin third component I_3 is $+\frac{1}{2}$ for up or anti-down quarks and $-\frac{1}{2}$ for down or an anti-up quarks, and the strangeness S is -1 for strange quarks and 1 for anti-strange quarks.

---

[2] The masses of the quarks enter the part of the Hamiltonian that describes the kinetic energy and the rest energy. The difference between the mass of an up/down quark and a strange quark is of the order $100\,\text{MeV}$, however, the binding energies in baryons typically range in the GeV range, so an approximate flavor symmetry can be assumed. For heavier quark flavors, this is no longer possible.

The mesons of both multiplets have zero orbital angular momentum but can attain two possible spin states: mesons with $S = 0$ are called "pseudoscalar", and mesons with $S = 1$ are called "vector" mesons.
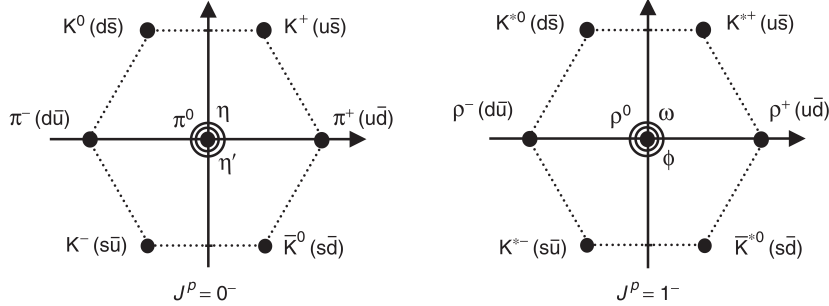

Figure 4.1: Multiplets of the pseudoscalar mesons (spin $S = 0$) and vector mesons (spin $S = 1$), plotted in terms of the isospin third component I_3 and the strangeness S. The mesons in the center are mixed states of $u\bar{u}$, $d\bar{d}$ and $s\bar{s}$. Figure taken from [21].

Table 4.1: Properties of the light mesons. Data taken from [22]. For some particles, the PDG only states the resonance width Γ. In that cases, the mean lifetime is calculated by $\tau = \hbar/\Gamma$. For the neutral kaons, no mean lifetime is given, as they are mixtures of the mass eigenstates K_S^0 and K_L^0 [3], where the first has a mean lifetime of $9.0 \cdot 10^{-11}$ s and the latter of $5.1 \cdot 10^{-8}$ s.

pseudoscalar mesons			vector mesons		
particle	mass	mean lifetime	particle	mass	mean lifetime
π^0	135 MeV	$8.5 \cdot 10^{-17}$ s	ρ^0	775 MeV	$4.5 \cdot 10^{-24}$ s
$\pi^\pm$	140 MeV	$2.6 \cdot 10^{-8}$ s	$\rho^\pm$	775 MeV	$4.5 \cdot 10^{-24}$ s
$K^\pm$	494 MeV	$1.2 \cdot 10^{-8}$ s	$K^{*\pm}$	892 MeV	$1.3 \cdot 10^{-23}$ s
$K^0, \bar{K}^0$	498 MeV	-	$K^{*0}, \bar{K}^{*0}$	896 MeV	$1.4 \cdot 10^{-23}$ s
η	548 MeV	$5.0 \cdot 10^{-19}$ s	ω	783 MeV	$7.8 \cdot 10^{-23}$ s
η'	958 MeV	$3.3 \cdot 10^{-21}$ s	ϕ	1 020 MeV	$1.6 \cdot 10^{-22}$ s

Table 4.1 shows the masses and mean lifetimes of the mesons, respectively. Pions are the lightest mesons and therefore appear most frequently in the experiment. The charged pions and kaons both have relatively long mean lifetimes as they decay via the weak interaction. Because of that, they are the only mesons that can be detected directly in the experiment and do not have to be reconstructed by their decay products [4]. The vector mesons, on the other hand, decay via the strong interaction and hence are very short-lived.

---

[3] The flavor eigenstates K^0 and $\bar{K}^0$ occurring in the pseudoscalar meson multiplet (Figure 4.1) oscillate between each other, a phenomenon known as "neutral kaon mixing". Hence, they do not have definite masses and lifetimes. Instead, K_S^0 ("K-short") and K_L^0 ("K-long") are the states with definite masses and lifetimes.

[4] Even though, about the half of the K^+ decays during their flight through the forward spectrometer and thus cannot be reconstructed at all.

4.4.2 Baryons

Figure 4.2 shows the two baryon multiplets. Like the mesons above, they have zero angular momentum but the quark spins can couple to a total spin of $S = \frac{1}{2}$ or $S = \frac{3}{2}$.

In Table 4.2, the properties of the baryons are listed. The proton is the only stable baryon. Free neutrons decay after about 15 minutes, however, if they are bound in a stable nucleus, they are also stable. Baryons containing one or more strange quarks are often called "hyperons" and abbreviated with a Y. Since strangeness is preserved by the electromagnetic and the strong interaction, ground-state hyperons can only decay weakly and therefore have a comparatively long mean lifetime of the order 10^{-10} s. The only exception is the Σ^0, which can decay electromagnetically via $\Sigma^0 \rightarrow \Lambda\gamma$, resulting in a nine orders of magnitude shorter lifetime. The Δ, Σ^* and Ξ^* particles are so-called baryon resonances, meaning they are short-lived (strongly decaying) excited states of their corresponding octet particles.
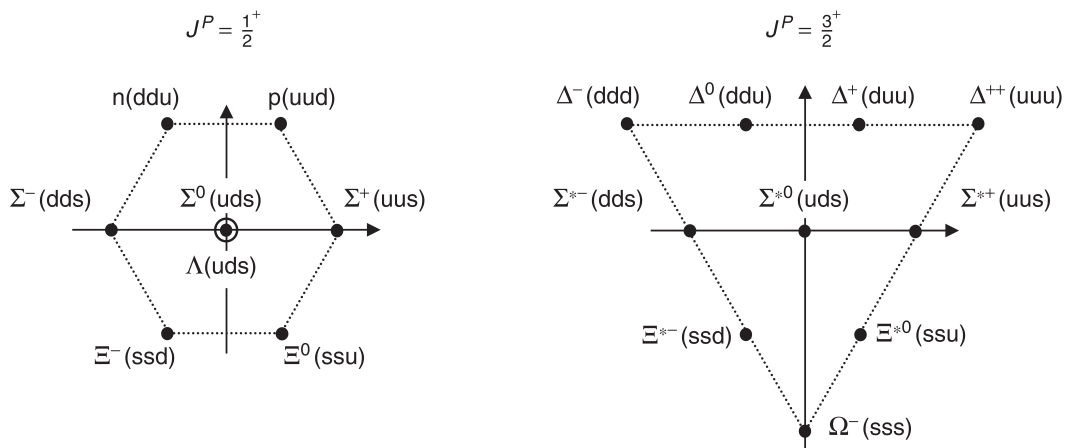

Figure 4.2: Multiplets of the light baryons with spin $S = \frac{1}{2}$ and $S = \frac{3}{2}$, plotted in terms of the isospin third component I_3 and the strangeness S. Figure taken from [21].

Table 4.2: Properties of the light baryons. Data taken from [22]. Like for the mesons, in cases where only the resonance width is stated, the mean lifetime is calculated by $\tau = \hbar/\Gamma$.

octet baryons			decuplet baryons		
particle	mass	mean lifetime	particle	mass	mean lifetime
p	938 MeV	stable	Δ	1 232 MeV	$5.6{\cdot}10^{-24}$ s
n	940 MeV	$8.8{\cdot}10^{2}$ s			
Λ	1 116 MeV	$2.6{\cdot}10^{-10}$ s			
Σ^+	1 189 MeV	$8.0{\cdot}10^{-11}$ s	Σ^{*+}	1 383 MeV	$1.8{\cdot}10^{-23}$ s
Σ^0	1 193 MeV	$7.4{\cdot}10^{-20}$ s	Σ^{*0}	1 384 MeV	$1.8{\cdot}10^{-23}$ s
Σ^-	1 197 MeV	$1.5{\cdot}10^{-10}$ s	Σ^{*-}	1 387 MeV	$1.7{\cdot}10^{-23}$ s
Ξ^0	1 315 MeV	$2.9{\cdot}10^{-10}$ s	Ξ^{*0}	1 532 MeV	$7.2{\cdot}10^{-23}$ s
Ξ^-	1 322 MeV	$1.6{\cdot}10^{-10}$ s	Ξ^{*-}	1 535 MeV	$6.6{\cdot}10^{-23}$ s
			Ω^-	1 672 MeV	$8.2{\cdot}10^{-11}$ s

Particle Reconstruction

5.1 Decay Diagrams

The basis for the reconstruction of the K^{*+} and the Y_{gs} is the knowledge of their decay paths, which are depicted in the decay diagrams in Figure 5.1. They are almost identical, except for an additional photon from the $\Sigma^0 \to \Lambda\gamma$ decay.
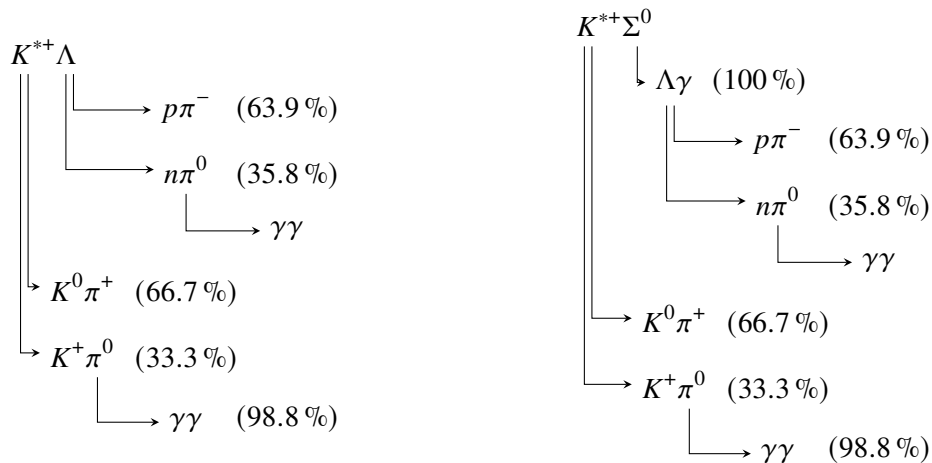
$K^{*+}\Lambda$

$\longrightarrow p\pi^-$ (63.9 %)

$\longrightarrow n\pi^0$ (35.8 %)

$\qquad\longrightarrow \gamma\gamma$

$\hookrightarrow K^0\pi^+$ (66.7 %)

$\hookrightarrow K^+\pi^0$ (33.3 %)

$\qquad\longrightarrow \gamma\gamma$ (98.8 %)

$K^{*+}\Sigma^0$

$\downarrow \Lambda\gamma$ (100 %)

$\longrightarrow p\pi^-$ (63.9 %)

$\longrightarrow n\pi^0$ (35.8 %)

$\qquad\longrightarrow \gamma\gamma$

$\longrightarrow K^0\pi^+$ (66.7 %)

$\longrightarrow K^+\pi^0$ (33.3 %)

$\qquad\longrightarrow \gamma\gamma$ (98.8 %)

Figure 5.1: Decay diagrams for the $K^{*+}Y_{\mathrm{gs}}$ states. The branching ratios given in parentheses are taken from [22].

In two thirds of the cases, the K^{*+} decays into $K^0\pi^+$ and in one third, it decays into $K^+\pi^0$. Nevertheless, it is sensible to reconstruct the K^{*+} from its less probable decay. The reason for that is that the K^0 is a mixing of the mass eigenstates K^0_S and K^0_L, where the latter most likely leaves the detector without being detected as it is uncharged and has a relatively long mean life time ($c\tau = 15.34\,\mathrm{m}$ [22]). The K^0_S, on the other hand, mostly decays into $\pi^+\pi^-$, which would result in a final state with at least three charged pions. As only the forward spectrometer is optimized for charged particle identification, it would be very difficult to reconstruct the K^{*+} from this channel.

The Λ decays into a pion and a nucleon. In both cases, it is practically impossible to reconstruct the Λ solely from its decay products: For the charged decay into $p\pi^-$, because only the forward spectrometer

is optimized for the identification of charged particles and it is very unlikely to measure more than one charged particle therein. And for the neutral decay into $n\pi^0$, because the neutron cannot be measured or at least not identified as such. Therefore, initially the K^{*+} is reconstructed and the Y_{gs} is obtained from the missing mass to the K^{*+}. To distinguish between Λ and Σ^0, the different E_γ thresholds and the photon from the $\Sigma^0 \rightarrow \Lambda\gamma$ decay can then be utilized, as detailed in sections 5.4 and 5.5.

5.2 Selection Cuts for Real Data Export

In this thesis, data from April/May 2017 is analyzed. The 6 cm long liquid hydrogen target was used during this beam time and in total about 2 billion events were recorded over a period of 22 days.

For the photoproduction of $K^{*+}\Lambda$ a photon beam of at least $E_\gamma = 1\,678$ MeV is necessary. This can be seen by the following calculation: If the K^{*+} and the Λ are produced at rest, then it follows from four-momentum conservation that

$$\left(p_\gamma + p_p\right)^2 = \left(p_{K^{*+}} + p_\Lambda\right)^2 \iff \left(E_\gamma + m_p\right)^2 - E_\gamma^2 = \left(m_{K^{*+}} + m_\Lambda\right)^2$$

$$\iff m_p^2 + 2E_\gamma m_p = \left(m_{K^{*+}} + m_\Lambda\right)^2$$

$$\iff E_\gamma = \frac{\left(m_{K^{*+}} + m_\Lambda\right)^2 - m_p^2}{2m_p} \approx 1\,678\,\text{MeV}.$$

The threshold for $K^{*+}\Sigma^0$ can be obtained analogously and amounts to $E_\gamma = 1\,846$ MeV. Hence, only those events were used for the analysis in which the photon beam energy amounts to at least $1\,600$ MeV. As described in the previous section, the K^{*+} shall be reconstructed via the $K^+\pi^0$ decay, so another requirement is that a K^+ has been detected in the forward spectrometer and at least two photons in the BGO.

In many events, there is no track in the forward spectrometer at all or less than two photons in the BGO, so the before-mentioned requirements already reduce the amount of data intensely to about 650 000 events.

5.3 Reconstruction of the K^{*+}

The first step of reconstructing the K^{*+} is to recreate the π^0 from photons in the BGO ball. Hence, for each event, every possible combination of two photons is built. In many cases, there are just two photons in the BGO, so there is only one possible combination. If the invariant mass of this combination lies between 100 and 160 MeV (assuming a Gaussian peak, this corresponds to approximately 3σ, see Figure A.1 in the appendix), it is assumed to be a π^0. In the general case of n photons in the BGO, $\frac{n^2-n}{2}$ combinations can be constructed of which $\lfloor\frac{n}{2}\rfloor$ represent a valid π^0 combination. Therefore only those combinations whose invariant mass is closest to the actual π^0 mass and still fits in the 100 to 160 MeV mass range are accepted as a valid π^0. The photons that are not used in a π^0 combination are marked as "single photons" and are referred to as γ' from now on. They are later used to identify the Σ^0.

After reconstructing the π^0, they can be combined with the K^+ from the forward spectrometer to obtain the K^{*+}. Of course, not all π^0 arise from the K^{*+} decay. Especially in real data, there are many other possible π^0 origins, resulting in a significant background contribution. But even in simulated data,
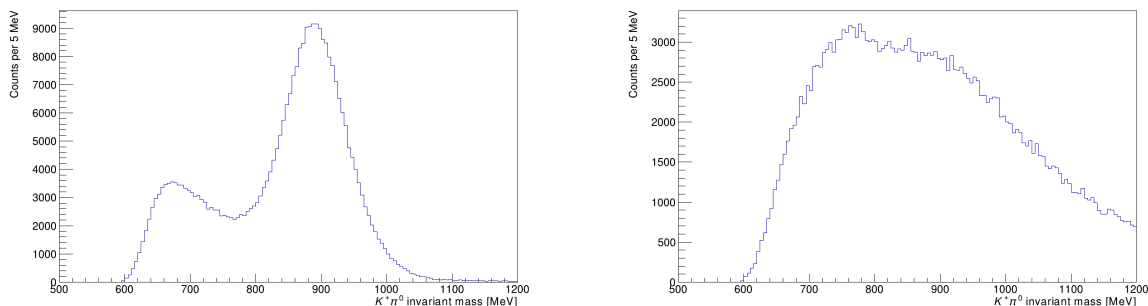
(a) $K^+\pi^0$ invariant mass for simulated $\gamma p \rightarrow K^{*+}\Lambda$ and $\gamma p \rightarrow K^{*+}\Sigma^0$ events. For each channel, 40 million events have been simulated. Around 900 MeV, the actual K^{*+} peak can be recognized, whereas between 600 and 800 MeV, another structure appears, originating from "false" combinations of a K^+ with a π^0 from the $\Lambda \rightarrow n\pi^0$ decay.

(b) $K^+\pi^0$ invariant mass for real data. A lot of other π^0 origins contribute here, resulting in a much broader spectrum where no K^{*+} peak can be seen.

Figure 5.2: Invariant mass of the $K^+\pi^0$ system.

there are π^0 from the Λ decay leading to "false" K^{*+} combinations. Therefore, the invariant mass of the $K^+\pi^0$ system is calculated to decide whether a combination is a valid K^{*+} or not.

Figures 5.2(a) and 5.2(b) show these invariant mass spectra for simulated and for real data, respectively. The invariant mass was required to lie between 800 and 1 000 MeV to accept the $K^+\pi^0$ system as a valid K^{*+}. Assuming the K^{*+} peak in Figure 5.2(a) follows a Gaussian distribution, that corresponds to approximately 2σ (see Figure A.2 in the appendix).

5.4 Reconstruction of the Y_{gs}

As mentioned previously, the Y_{gs} is reconstructed via the K^{*+} missing mass. Figure 5.3 displays the missing mass to $K^+\pi^0$ systems identified as K^{*+}. The histograms should peak in proximity to the Λ and Σ^0 masses, between 1 100 and 1 200 MeV, and indeed, that is the case for both simulated and real data. For real data, the peak expectedly sits on top of a vast background, but it is surprising that it can already be seen at all without further requirements.

### Requirement of an Additional π^0 from Λ Decay

A sensible next step in the analysis is to require an additional π^0 from the neutral Λ decay and examine the missing mass to the K^{*+} and this pion, which should correspond to the neutron mass. Specifically, this means that all $K^+\pi^0$ combinations identified as a K^{*+}, and all other π^0 that have not already been used in those combinations, are combined together, and their missing mass is calculated. The result is depicted in Figure 5.4.

The histograms now have significantly fewer entries compared to those in Figure 5.2 and Figure 5.3. The reason for this is that the branching ratio for $\Lambda \rightarrow n\pi^0$ is only 35.8 % (see Figure 5.1), and in addition, it is not very likely to observe all four photons from the two π^0 decays. Even if all four photons are observed, their energies might not be measured accurately, or they might not be correctly combined
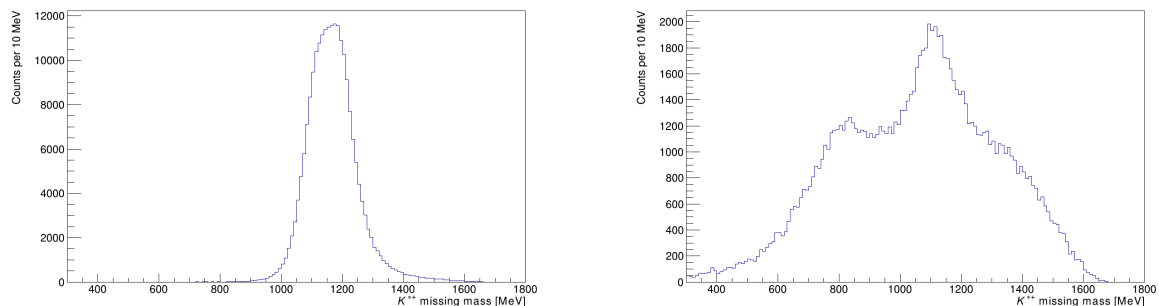
(a) Simulated data. A clear peak around 1 150 MeV can be seen, right between the Λ and Σ^0 masses.

(b) Real data. Here too, a peak between the Λ and Σ^0 masses is noticeable, standing out from the background.

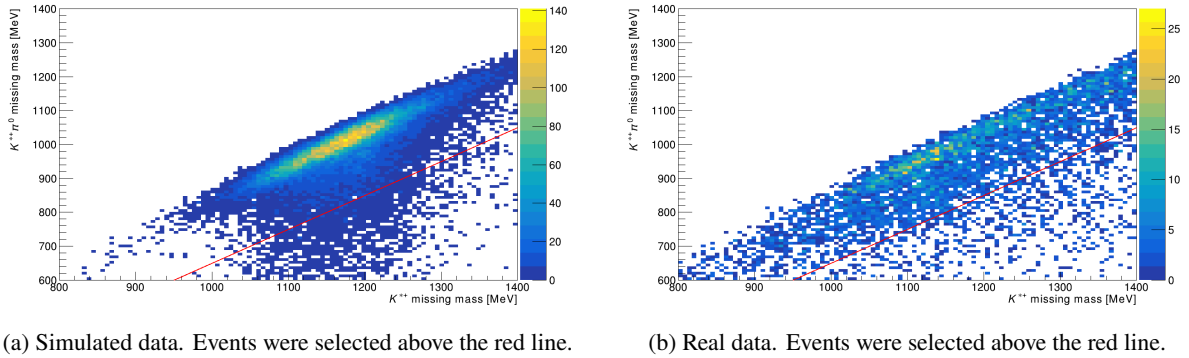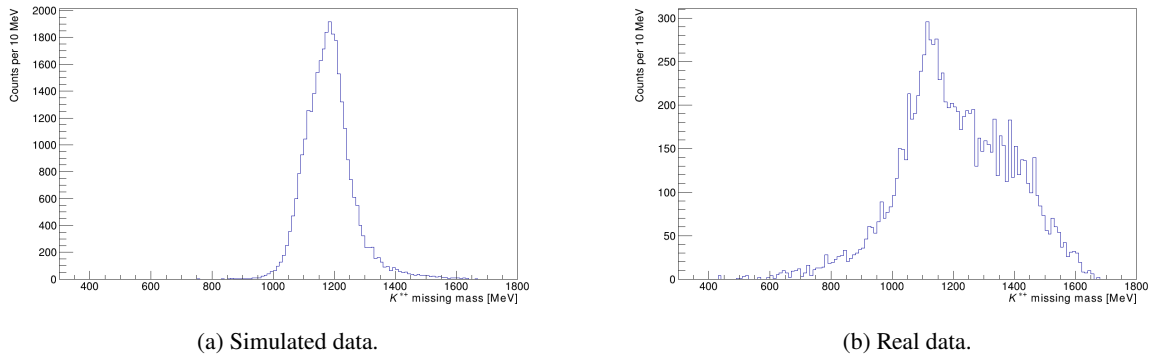Figure 5.3: Missing mass to the K^{*+}.
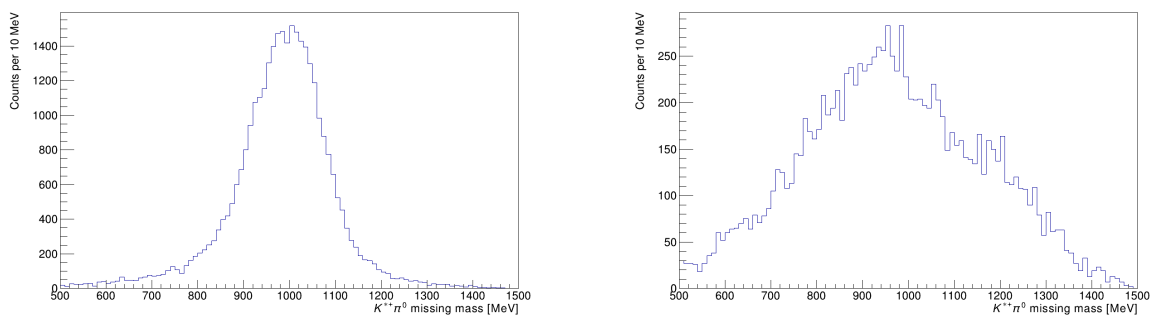
(a) Simulated data.

(b) Real data.

Figure 5.4: Missing mass to the $K^{*+}\pi^0$ system.

to form the π^0 during the analysis. As a result, the peaks in these histograms are much broader than in previous ones. Nevertheless, the peaks are approximately located at the neutron mass of 938 MeV, as expected.

Applying a Two-dimensional Cut

A first goal of the further analysis is to remove background in the K^{*+} missing mass histogram to sharpen the Y_{gs} peak. One opportunity to do this would be to require an additional π^0 like in the previous section and to apply a cut directly in the $K^{*+}\pi^0$ missing mass histogram. However, it is more reasonable to look into a two-dimensional histogram in which the $K^{*+}\pi^0$ missing mass is plotted against the K^{*+} missing mass.

Such histograms are displayed in Figure 5.5. The missing mass of the $K^{*+}\pi^0$ system must be at least 135 MeV less than the K^{*+} missing mass. That is why all data points occur below the diagonal. In both simulated and real data a blob can be seen extending from about 1 100 to 1 200 MeV in x direction and from about 900 to 1 100 MeV in y direction. Data points that lie clearly outside this region most likely do not originate from the searched-for reactions and therefore can be sorted out. Therefore, only the events were selected in which the $K^{*+}\pi^0$ missing mass is at least 350 MeV greater than the K^{*+} missing

(a) Simulated data. Events were selected above the red line.

(b) Real data. Events were selected above the red line.

Figure 5.5: Missing mass to the $K^{*+}\pi^0$ system versus missing mass to the K^{*+}.

(a) Simulated data.

(b) Real data.

Figure 5.6: Missing mass to the K^{*+} after the two-dimensional cut.

mass. These are the data points above the red line.

After applying this two-dimensional cut, the K^{*+} missing mass can be plotted again. The result is depicted in Figure 5.6. Especially for real data, a clear improvement compared to the corresponding histogram in Figure 5.3 can be noticed: Most of the background on the left side of the peak has vanished.

Beam Energy Dependence

The K^{*+} missing mass spectrum depends on the energy E_γ of the photon beam. This can be seen by plotting E_γ versus the K^{*+} missing mass of the previously selected events in a two-dimensional histogram, which is shown in Figure 5.7. Especially in simulated data, it can be observed that the K^{*+} missing mass peak is most pronounced close to threshold, while with higher photon beam energy, the background increases and the peak becomes more diffuse.

Therefore, it is sensible to plot the K^{*+} missing mass again for various beam energy intervals. The results are depicted in Figures A.3 and A.4 in the appendix. The plots in the first row are particularly of interest, as in this energy range, there are only few background contributions. For higher energies, however, significantly fewer $K^{*+}Y_{gs}$ events appear, as can be seen in simulated data, and more background influences come into play, as shown by the real data. As a result, the peaks become lower and broader, and, at least in real data, may eventually not be discernible anymore.
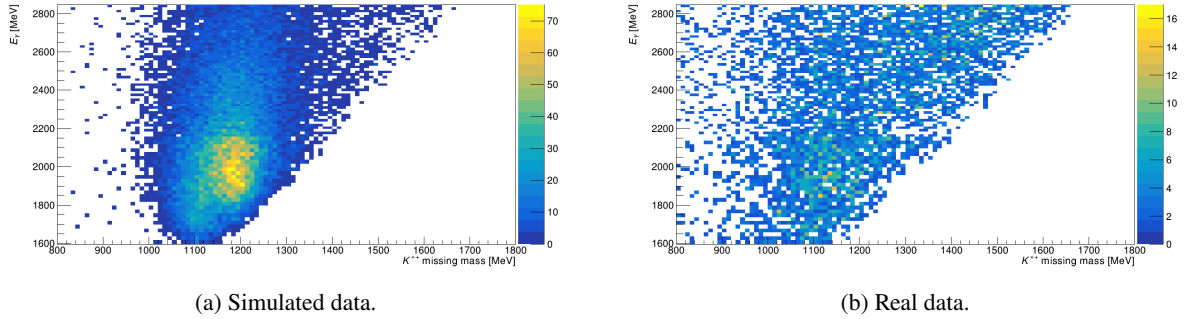
(a) Simulated data.

(b) Real data.

Figure 5.7: Photon beam energy E_γ versus missing mass to the K^{*+}.
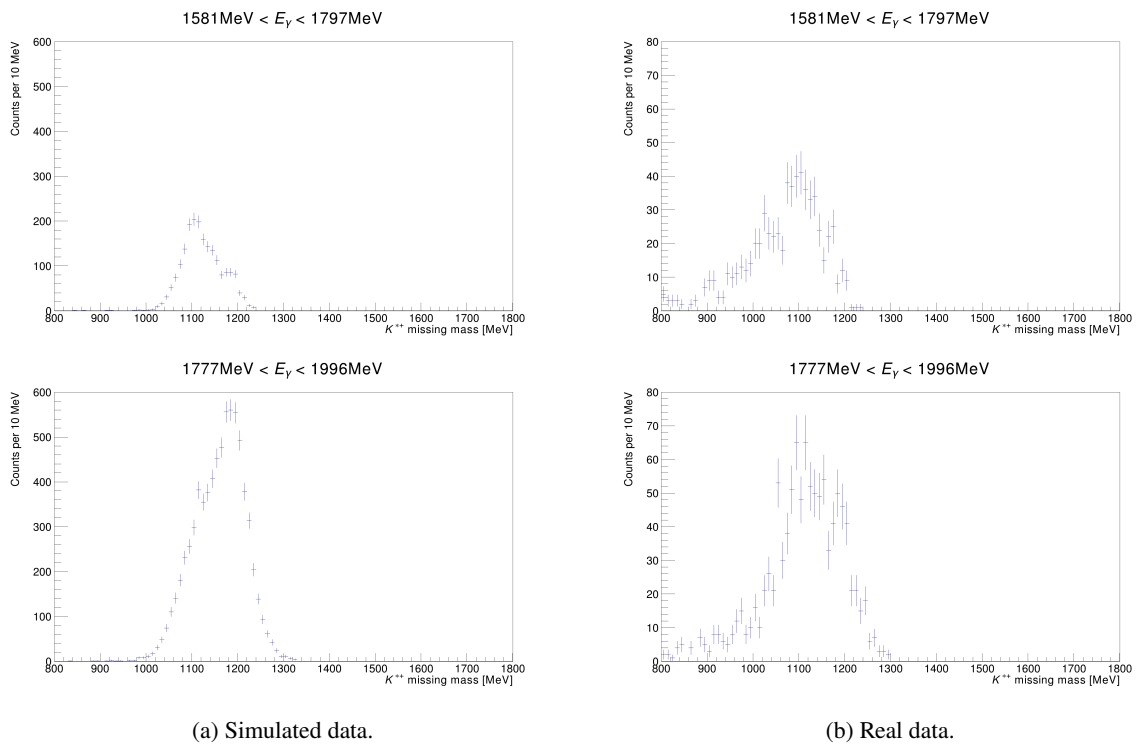

(a) Simulated data.

(b) Real data.

Figure 5.8: Missing mass to the K^{*+} for two different energy ranges close to the $K^{*+}\Lambda$ and the $K^{*+}\Sigma^0$ thresholds.

The content of the first four histograms from Figures A.3 and A.4 is depicted again in Figure 5.8 for two different energy ranges. The $K^{*+}\Lambda$ threshold ($E_\gamma = 1\,678\,\text{MeV}$) lies in the first energy interval, while the $K^{*+}\Sigma^0$ threshold ($E_\gamma = 1\,846\,\text{MeV}$) is only reached in the next interval. Consequently, the peaks in the upper histograms are centered around the Λ mass, whereas in the lower histograms, a second peak can be observed at the Σ^0 mass. In simulated data, the Σ^0 peak is even higher than the Λ peak, which is not the case for real data. This implies that, unlike in simulated data where 40 million events were simulated for each of $K^{*+}\Lambda$ and $K^{*+}\Sigma^0$, in reality, the two reactions do not occur in the same proportion. Instead, photoproduction of $K^{*+}\Lambda$ seems to be clearly preferred.

In Figure 5.8, it can be clearly seen that the $K^{*+}\Lambda$ and $K^{*+}\Sigma^0$ events can be distinguished based on their thresholds, and both peaks can be resolved for beam energies near the thresholds. However, they are closely spaced and overlap with each other. Another criterion for distinguishing them can therefore be the characteristic $\Sigma^0 \rightarrow \Lambda\gamma$ decay.

5.5 Distinction of Λ and Σ^0

The Σ^0 decays into $\Lambda\gamma$ with a branching ratio of almost $100\,\%$ [22]. In the Σ^0 rest frame, the decay particles fly back-to-back with the same momentum $|\mathbf{p}| = E_{\gamma'}$. Hence, the energy of the Λ is $E_\Lambda = \sqrt{m_\Lambda^2 + E_{\gamma'}^2}$ and due to energy conservation, one finds for the energy $E_{\gamma'}$ of the single photon:

$$m_{\Sigma^0} = E_{\gamma'} + E_\Lambda = E_{\gamma'} + \sqrt{m_\Lambda^2 + E_{\gamma'}^2}$$
$$\Longleftrightarrow m_{\Sigma^0}^2 + E_{\gamma'}^2 - 2m_{\Sigma^0}E_{\gamma'} = m_\Lambda^2 + E_{\gamma'}^2$$
$$E_{\gamma'} = \frac{m_{\Sigma^0}^2 - m_\Lambda^2}{2m_{\Sigma^0}} \approx 75\,\text{MeV}$$

This characteristic can be used to distinguish between Λ and Σ^0. Namely, the idea is to boost the single photons γ' (those that have not been used in π^0 combinations) into the rest frame of the Y_{gs}. Figure 5.9 displays the $K^{*+}\gamma'$ missing mass versus the single photon energy $E_{\gamma'}$ in the Y_{gs} rest frame. If the Y_{gs} corresponds to a Σ^0, then $E_{\gamma'}$ should be close to the above-mentioned 75 MeV, and the $K^{*+}\gamma'$ missing mass should be close to the Λ mass. Indeed, in simulated data, a clear peak is discernible in this region. In real data, there is much less statistics, resulting in a less pronounced but nevertheless visible peak. Based on the histograms, cuts of $60\,\text{MeV} < E_{\gamma'} < 90\,\text{MeV}$ and $1\,000\,\text{MeV} < \text{MM}(K^{*+}\gamma') < 1\,200\,\text{MeV}$ were chosen, indicated by the red lines. If an event falls into this region, it is assumed to originate from a $K^{*+}\Sigma^0$ reaction.

After this cut, the K^{*+} missing mass can be plotted again. The result is shown in Figure 5.10 for the same energy ranges as in Figure 5.8. In the upper plot, which previously contained almost exclusively $K^{*+}\Lambda$ events due to the thresholds, there is now no distinct peak visible, as the $K^{*+}\Lambda$ events have been predominantly removed by the last cut. In the lower plot, the peak at the Σ mass has become more prominent, while the Λ peak, at least in simulated data, has almost disappeared. In real data, there are still some $K^{*+}\Lambda$ events that passed the cut, causing a peak at the Λ mass. However, the Σ^0 peak has become much more distinct compared to Figure 5.8.

(a) Simulated data. Events were selected between the red lines.

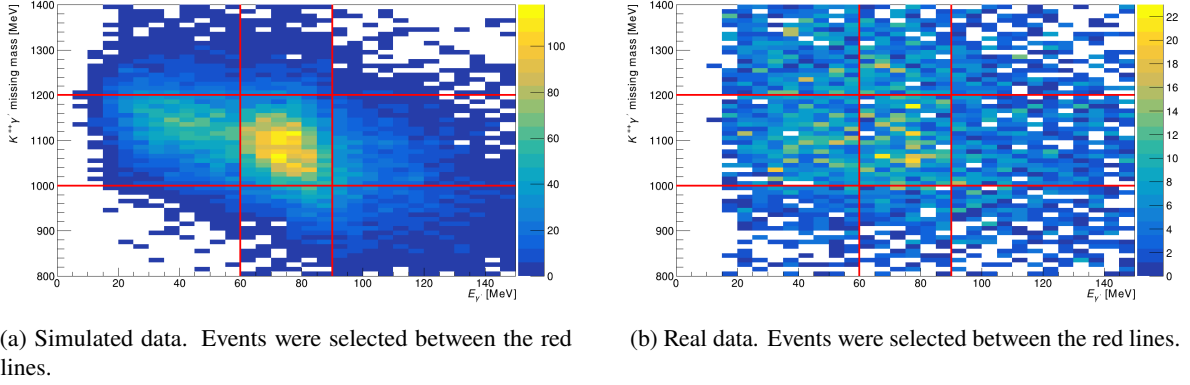(b) Real data. Events were selected between the red lines.

Figure 5.9: Missing mass to the $K^{*+}\gamma'$ system versus energy $E_{\gamma'}$ of single photons in the Y_{gs} rest frame.
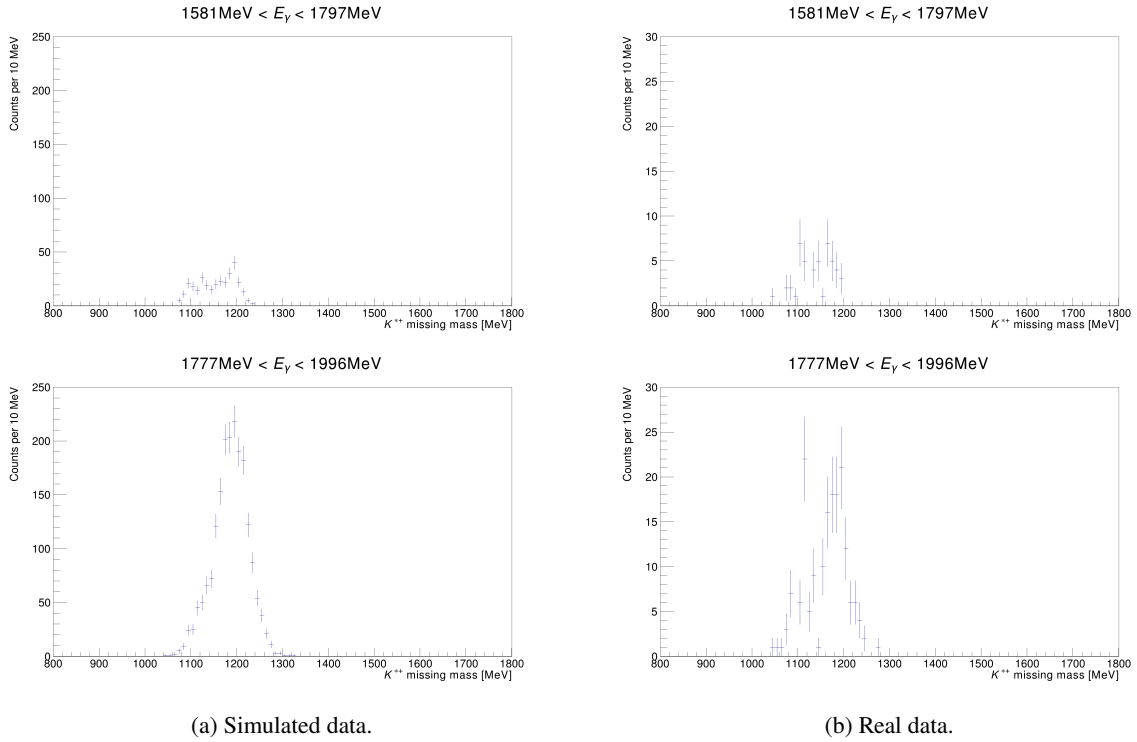

(a) Simulated data.

(b) Real data.

Figure 5.10: Missing mass to the K^{*+} for two different energy ranges after selecting $K^{*+}\Sigma^0$ events.

Outlook: Cross Section Determination

In the previous chapter, particles have been reconstructed by various requirements and selection cuts. The results are histograms in which the investigated particle reactions can be identified. As a next step, one is usually interested in the cross section for the respective reaction, which is a measure of its probability. The cross section does not depend on the experimental setup and is therefore used to compare data from different experiments.

The determination of the cross section requires knowing the exact number of events in which the $\gamma p \to K^{*+} Y_{\text{gs}}$ reaction occurs. Despite applying all selection cuts, there is still some background present from other channels in the final K^{*+} missing mass plots in Figure 5.8. To estimate their contributions, each background channel needs to be simulated, processed through the analysis, and then fitted to the missing mass histograms. This process is rather time-consuming and therefore was not performed as a part of this thesis. However, this work can serve as a foundation for a future cross section determination. Hence, this chapter briefly outlines how the cross section is defined and how it can be determined based on this work.

6.1 Definition of the Cross Section

For a certain particle reaction, the reaction rate $\dot{N}$ equals the product of the cross section σ and the luminosity $\mathcal{L}$ [23]:

$$\dot{N} = \sigma \cdot \mathcal{L} \tag{6.1}$$

The luminosity quantifies how many collisions of beam and target particles happen per unit time and area. Given a beam of particles of type a incident upon a fixed target of particles of type b, the luminosity is the product of the number of target particles N_b and the flux $\Phi_a = \dot{N}_a/A$, where A is the cross sectional area of the beam. Inherently, the luminosity depends on the experimental setup, particularly on the accelerator. The cross section, on the other hand, is a measure of how likely a particle reaction is and is independent of the accelerator and the detector.

By integrating equation 6.1 one gets the following formula for the cross section:

$$N = \sigma \cdot \int \mathcal{L} \, \mathrm{d}t = \sigma \cdot N_a \cdot n_b \cdot d \qquad \Longleftrightarrow \qquad \sigma = \frac{N}{N_a \cdot n_b \cdot d} \tag{6.2}$$

In this context, N_a represents the total number of incident beam particles, n_b denotes the particle number density of the target particles, and d stands for the length of the target.

The cross section usually varies strongly with the angle θ under which the final state particles arise, and the center-of-mass energy W available for particle production. Therefore, one is normally interested in the differential cross section $\frac{d\sigma}{d\Omega}$, where $d\Omega = d\phi \sin\theta d\theta$, as a function of W. In the case of photoproduction off the proton, one can also consider the differential cross section as a function of beam energy E_γ, as W and E_γ are related by

$$W = \sqrt{m_p^2 + 2m_p E_\gamma},$$

where m_p is the proton mass.

6.2 Calculation of the Cross Section

Based on equation 6.2, the differential cross section of the investigated $\gamma p \to K^{*+}Y_{gs}$ reactions can be obtained with the following formula.

$$\frac{d\sigma(\theta, E_\gamma)}{d\Omega} = \frac{N(\theta, E_\gamma)}{\varepsilon(\theta, E_\gamma) \cdot N_\gamma(E_\gamma) \cdot n_p \cdot d \cdot \Delta\Omega} \tag{6.3}$$

The quantities appearing in the formula have the following meanings:

- $N(\theta, E_\gamma)$ is the number of events identified with the respective $\gamma p \to K^{*+}Y_{gs}$ reaction through the analysis. To properly determine this number, the before-mentioned fitting of background contributions needs to be done.

- $\varepsilon(\theta, E_\gamma)$ is the so-called reconstruction efficiency. It is defined as the fraction of events identified as the sought-after reaction, compared to the actual number of these reactions. Since the latter is unknown in real data, it has to be determined with simulated data. The fraction $N(\theta, E_\gamma)/\varepsilon(\theta, E_\gamma)$ then yields the actual amount of $\gamma p \to K^{*+}Y_{gs}$ reactions.

- $N_\gamma(E_\gamma)$ is the photon flux, i.e. the (integrated) number of photons with an energy E_γ impinging the target. It is detected by FluMo as described in section 3.5 and is depicted in Figure A.5 in the appendix.

- n_p is the particle number density of protons inside the target. It is calculated by

$$n_p = \frac{\rho \cdot N_A}{M(H)}, \tag{6.4}$$

where ρ is the density of liquid hydrogen ($\rho = 0.07085\,\mathrm{g\,cm^{-3}}$ at its normal boiling point $T = 20.369\,\mathrm{K}$ [24]), N_A is Avogadro's constant ($N_A = 6.02214076 \cdot 10^{23}\,\mathrm{mol^{-1}}$ [25]) and $M(H)$ is the molar mass of hydrogen ($M(H) = 1.0080(2)\,\mathrm{g\,mol^{-1}}$ [26]).

- d is the length of the target ($d = 6\,\mathrm{cm}$).

- $\Delta\Omega$ is the solid angle range in which the final state particles were observed. Strictly speaking, this range must be infinitesimally small to actually get the *differential* cross section $\frac{d\sigma}{d\Omega}$. However, in

24

practice, it is sufficient to consider a small region $\Delta\Omega$ in which the cross section does not change significantly. Generally, the cross section is independent of the azimuthal angle ϕ, so the solid angle range can be calculated by

$$\Delta\Omega = \int_0^{2\pi} \mathrm{d}\phi \int_{\theta_1}^{\theta_2} \sin\theta \, \mathrm{d}\theta = 2\pi \cdot \left[\cos\theta\right]_{\theta_1}^{\theta_2}. \tag{6.5}$$

In summary, a recipe for determining the differential cross section for $\gamma p \to K^{*+} Y_{\mathrm{gs}}$ based on the previous results would look as follows:

First, the influences of background channels on the K^{*+} missing mass histograms would need to be studied and fitted. Possible background channels include, for example, $\gamma p \to K^+ \Sigma(1385)$, $\gamma p \to K^+ \Lambda(1405)$, and $\gamma p \to K^+ \Lambda(1520)$, as the $\Sigma(1385)$, $\Lambda(1405)$, and $\Lambda(1520)$ can each decay into $\Lambda\pi^0$ or $\Sigma^0\pi^0$, resulting in the same particles in the final state as in $K^{*+} Y_{\mathrm{gs}}$ photoproduction.

After that, the full angular range would need to be divided into smaller regions, and for each region, the number of reactions N, the reconstruction efficiency ε, and the solid angle $\Delta\Omega$ need to be determined to finally calculate the cross section using equation 6.3.

To make a reasonable choice for that angular regions, it is necessary to examine the $\cos\theta_{\mathrm{CM}}^{K^{*+}}$ distribution, which is depicted in Figure 6.1. As the K^+ was required to be measured in the forward spectrometer, the angles of the reconstructed K^{*+} are mostly forward-distributed. However, sometimes the π^0 takes so much of the K^{*+} momentum that, at least in the center-of-mass frame, it occurs under a backward angle.
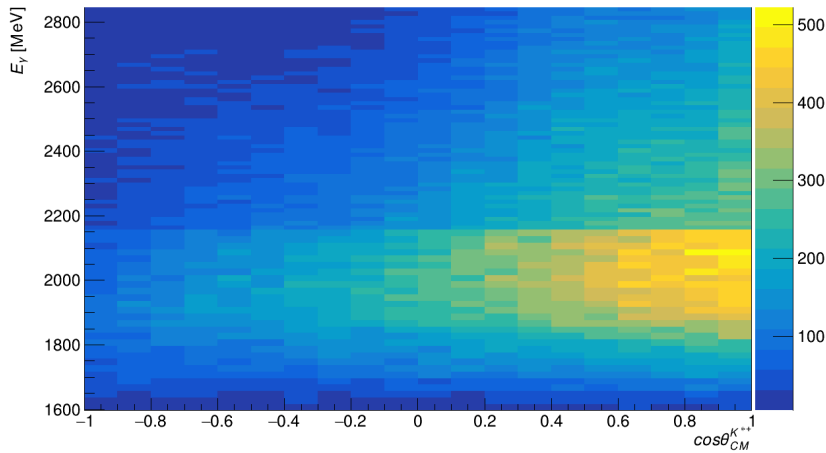
Figure 6.1: Photon beam energy E_γ versus $\cos\theta_{\mathrm{CM}}^{K^{*+}}$ for simulated data. As in Chapter 5, 40 million events were simulated for $\gamma p \to K^{*+}\Lambda$ and $\gamma p \to K^{*+}\Sigma^0$, respectively. In most cases, the reconstructed K^{*+} is forward-directed, as the K^+ was required to be measured in the forward spectrometer.

Since there are relatively few events where the reconstructed K^{*+} appears at an angle of $\cos\theta_{\mathrm{CM}}^{K^{*+}} < 0$, determining the cross-section in this angular range is not meaningful. Due to the poor statistics, the errors are expected to be comparatively large. Instead, when determining the differential cross-section, one should focus on positive intervals of $\cos\theta_{\mathrm{CM}}^{K^{*+}}$ (for example, $1.0 > \cos\theta_{\mathrm{CM}}^{K^{*+}} > 0.8$, $0.8 > \cos\theta_{\mathrm{CM}}^{K^{*+}} > 0.6$, ...).

25

Summary

The main result of this thesis is that the observation of $K^{*+}Y_{\text{gs}}$ photoproduction is possible with the BGOOD experiment. The $K^{*+}\Lambda$ and $K^{*+}\Sigma^0$ channels were successfully reconstructed in the analysis and could even be distinguished based on their distinct energy thresholds and the characteristic photon arising from the $\Sigma^0 \to \Lambda\gamma$ decay.

The first step of the analysis involved reconstructing the K^{*+} through its $K^+\pi^0$ decay, with the K^+ being measured in the forward spectrometer and the π^0 in the BGO ball. Then, the Y_{gs} was obtained by the missing mass to K^{*+} and by requiring a second π^0 from the Λ decay. This requirement and the subsequent cuts removed most of the background from other channels but significantly reduced the amount of data. In this context, an interesting question for possible future investigations would be whether the reconstruction of the Λ via a proton in the BGO or in SciRi would be similarly effective, and perhaps fewer actual $K^{*+}Y_{\text{gs}}$ events would be lost. Finally, the $K^{*+}\Lambda$ and the $K^{*+}\Sigma^0$ reactions could be identified by plotting the K^{*+} missing mass for beam energies close to their thresholds. The requirement of a single photon from the $\Sigma^0 \to \Lambda\gamma$ decay then allowed for a further distinction between the Λ and the Σ^0.

A next step in a full analysis of the $\gamma p \to K^{*+}\Lambda$ and the $\gamma p \to K^{*+}\Sigma^0$ channels would be the determination of their differential cross sections as described in Chapter 6. Their determination is worthwhile as the differential cross sections could contain hints of possible unconventional structures in the light quark sector, as stated in the motivation of this thesis.

Additional Histograms
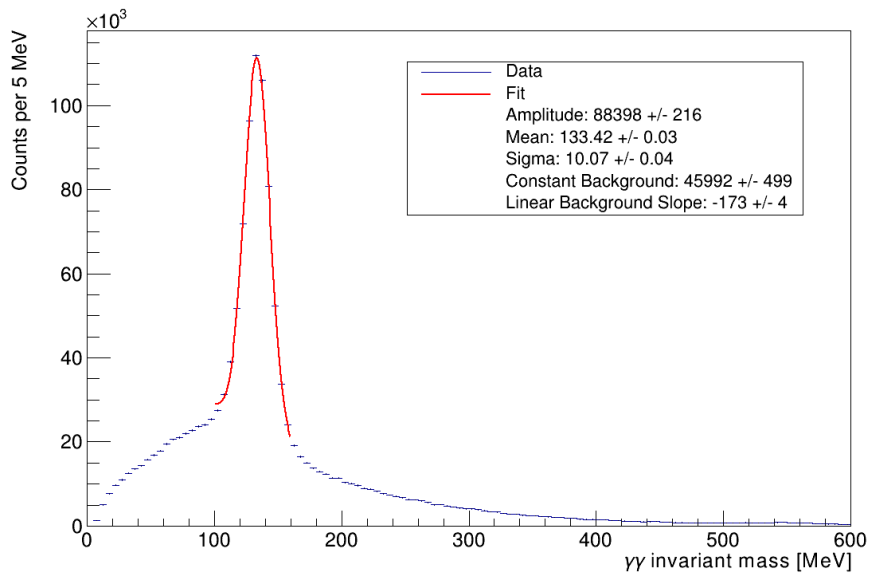
Figure A.1: 2γ invariant mass in the BGO for real data. The peak was fitted with a Gaussian curve along with a linear function as background. The fitting results are listed in the legend. The mean value of 133 MeV is consistent with the π^0 mass of 135 MeV. The invariant mass range from 100 to 160 MeV, where 2γ combinations are accepted as valid π^0, corresponds approximately to a 3σ interval.
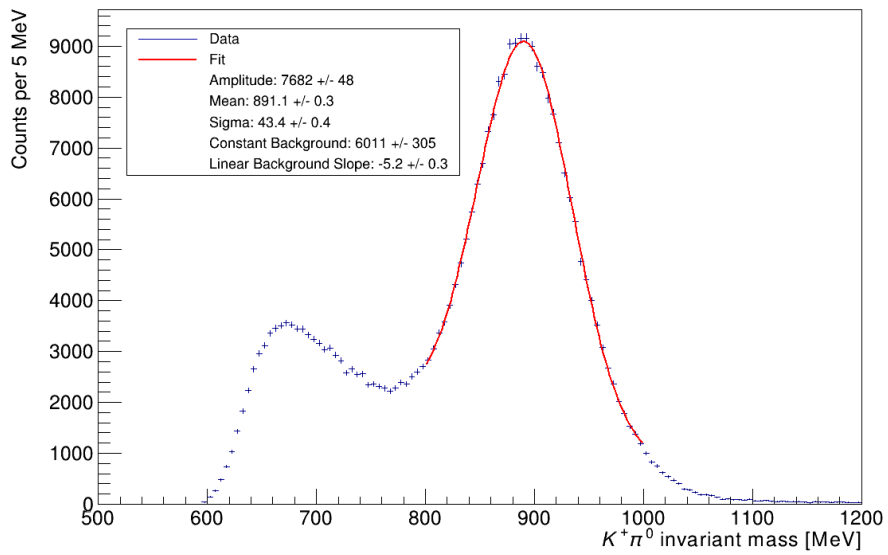
Figure A.2: $K^+\pi^0$ invariant mass for simulated data. Again, the peak was fitted with a Gaussian curve along with a linear function as background. The fitting results are listed in the legend. The mean value of 891 MeV is consistent with the K^{*+} mass of 892 MeV. The invariant mass range from 800 to 1 000 MeV, where $K^+\pi^0$ combinations are accepted as valid K^{*+}, corresponds approximately to a 2σ interval.
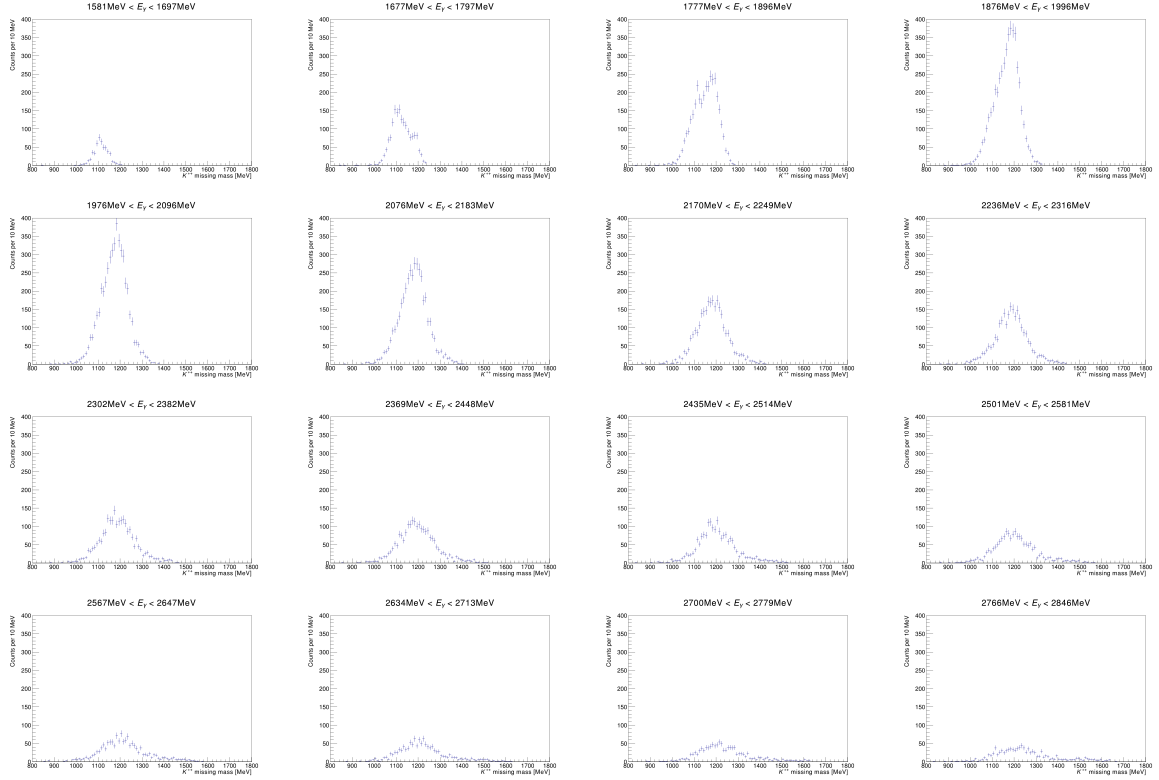
Figure A.3: Missing mass to the K^{*+} for simulated data for various photon beam energies, labelled at the top of each histogram. The energy ranges are based on the binning of the photon tagger, with each histogram covering five tagger bins. Close to threshold, the peaks are the highest and the narrowest, becoming lower and broader with higher photon beam energy. In the first row it can be seen how the peak slightly moves to the right beyond the $K^{*+}\Sigma^0$ threshold ($E_\gamma = 1\,846$ MeV): In the first two histograms, almost exclusively $K^{*+}\Lambda$ events contribute, whereas from the third histogram onward, where the threshold is reached, the peak becomes more centered around the Σ^0 mass.
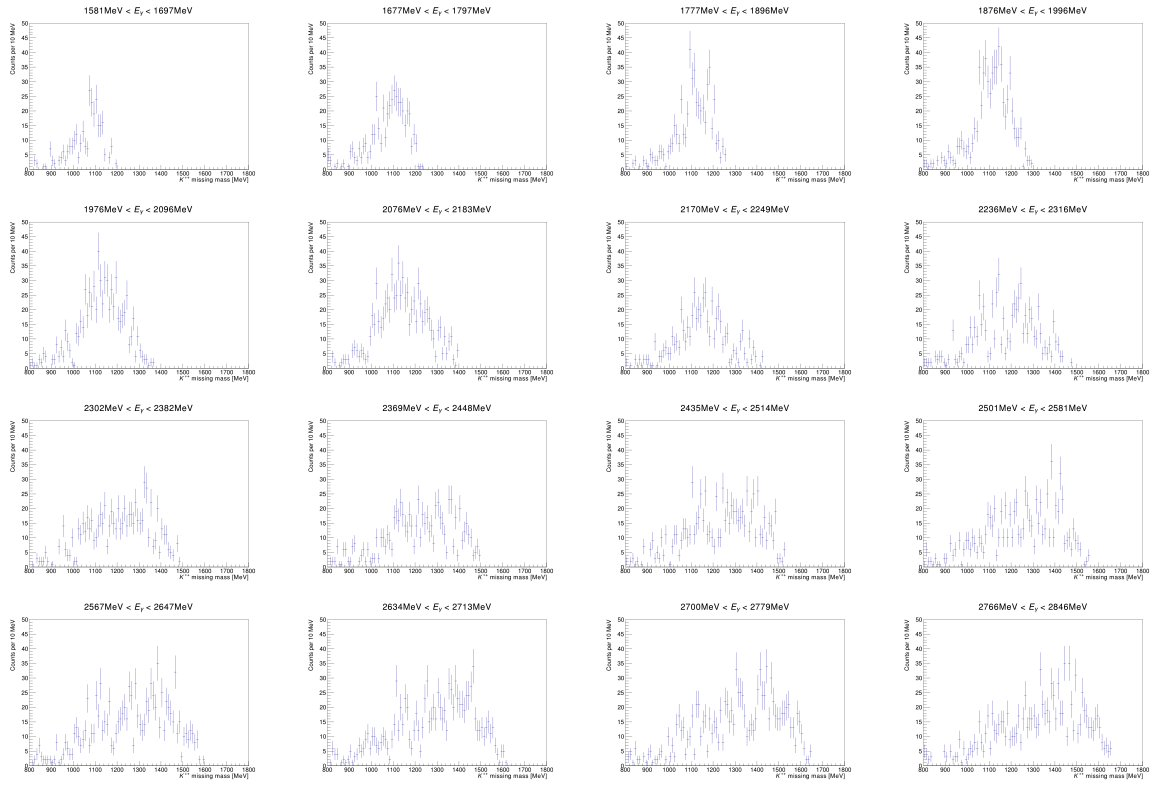
Figure A.4: Missing mass to the K^{*+} for real data for various photon beam energies, labelled at the top of each histogram. For $E_\gamma > 2\,300\,\text{MeV}$ (last two rows), no clear peak can be seen anymore, since contrary to simulated data, several other background channels contribute here.
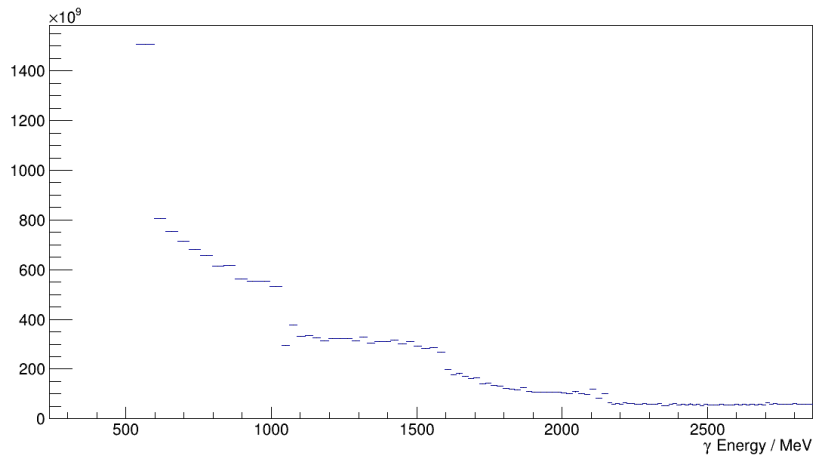
Figure A.5: Photon flux as a function of beam energy, measured by FluMo.

Bibliography

[1] H.-X. Chen, W. Chen, X. Liu and S.-L. Zhu, *The hidden-charm pentaquark and tetraquark states*, Physics Reports **639** (2016) 1, ISSN: 0370-1573, URL: https://www.sciencedirect.com/science/article/pii/S037015731630103X (cit. on pp. 1, 3).

[2] R. Ewald et al., *Anomaly in the $K_S^0 \Sigma^+$ photoproduction cross section off the proton at the K^* threshold*, Physics Letters B **713** (2012) 180, ISSN: 0370-2693, URL: https://www.sciencedirect.com/science/article/pii/S0370269312006259 (cit. on pp. 1, 3, 4).

[3] T. Jude et al., *Observation of a cusp-like structure in the $\gamma p \rightarrow K^+ \Sigma^0$ cross section at forward angles and low momentum transfer*, Physics Letters B **820** (2021) 136559, ISSN: 0370-2693, URL: https://www.sciencedirect.com/science/article/pii/S0370269321004998 (cit. on pp. 1, 4, 5).

[4] Cush, *The Standard Model of Elementary Particles*, URL: https://commons.wikimedia.org/w/index.php?curid=4286964 (visited on 02/09/2022) (cit. on p. 3).

[5] Belle Collaboration, *Observation of a Narrow Charmoniumlike State in Exclusive $B^\pm \rightarrow K^\pm \pi^+ \pi^- J/\psi$ Decays*, Phys. Rev. Lett. **91** (26 2003) 262001, URL: https://link.aps.org/doi/10.1103/PhysRevLett.91.262001 (cit. on p. 2).

[6] BABAR Collaboration, *Observation of the Decay $B \rightarrow J/\psi \eta K$ and Search for $X(3872) \rightarrow J/\psi \eta$*, Phys. Rev. Lett. **93** (4 2004) 041801, URL: https://link.aps.org/doi/10.1103/PhysRevLett.93.041801 (cit. on p. 2).

[7] LHCb Collaboration, *Observation of X(3872) production in pp collisions at $\sqrt{s} = 7$ TeV*, The European Physical Journal C **72** (2012) 1972, ISSN: 1434-6052, URL: https://doi.org/10.1140/epjc/s10052-012-1972-7 (cit. on p. 2).

[8] LHCb Collaboration, *Observation of $J/\psi p$ Resonances Consistent with Pentaquark States in $\Lambda_b^0 \rightarrow J/\psi K^- p$ Decays*, Phys. Rev. Lett. **115** (7 2015) 072001, URL: https://link.aps.org/doi/10.1103/PhysRevLett.115.072001 (cit. on p. 3).

[9] LHCb Collaboration, *Observation of a Narrow Pentaquark State, $P_c(4312)^+$, and of the Two-Peak Structure of the $P_c(4450)^+$*, Phys. Rev. Lett. **122** (22 2019) 222001, URL: https://link.aps.org/doi/10.1103/PhysRevLett.122.222001 (cit. on p. 3).

[10] *MAID*, URL: https://maid.kph.uni-mainz.de/ (visited on 22/02/2024) (cit. on p. 3).

[11] *SAID*, URL: https://gwdac.phys.gwu.edu/ (visited on 22/02/2024) (cit. on p. 3).

[12] A. Ramos and E. Oset, *The role of vector-baryon channels and resonances in the $\gamma p \to K^0\Sigma^0$ and $\gamma n \to K^0\Sigma^0$ reactions near the $K^*\Lambda$ threshold*, Physics Letters B **727** (2013) 287, ISSN: 0370-2693, URL: https://www.sciencedirect.com/science/article/pii/S0370269313008058 (cit. on p. 3).

[13] Kohl, K. et al., *Measurement of the $\gamma n \to K^0\Sigma^0$ differential cross section over the K^* threshold*, Eur. Phys. J. A **59** (2023) 254, URL: https://doi.org/10.1140/epja/s10050-023-01133-1 (cit. on p. 4).

[14] A. Anisovich et al., *Energy-independent PWA of the reaction $\gamma p \to K^+\Lambda$*, The European Physical Journal A **50** (2014), URL: https://doi.org/10.1140/epja/i2014-14129-3 (cit. on p. 5).

[15] Alef, S. et al., *The BGOOD experimental setup at ELSA*, Eur. Phys. J. A **56** (2020) 104, URL: https://doi.org/10.1140/epja/s10050-020-00107-x (cit. on pp. 6, 8, 9).

[16] ELSA, *Setup of ELSA*, URL: https://www-elsa.physik.uni-bonn.de/elsa.html (visited on 09/02/2024) (cit. on pp. 6, 7).

[17] O. Freyermuth, *Studies of ω Photoproduction off Proton at the BGO-OD Experiment*, PhD Thesis: University of Bonn, 2017, URL: https://hdl.handle.net/20.500.11811/7263 (cit. on p. 11).

[18] *ROOT*, URL: https://root.cern.ch/ (visited on 03/06/2024) (cit. on p. 11).

[19] K. Kohl, *Measurement of the $\gamma n \to K^0\Sigma^0$ photoproduction at the BGOOD experiment and the relation to possible pentaquark states*, PhD Thesis: University of Bonn, 2021, URL: https://hdl.handle.net/20.500.11811/9736 (cit. on p. 11).

[20] S. Agostinelli et al., *GEANT4-a simulation toolkit*, Nuclear Instruments and Methods in Physics Research Section A: Accelerators, Spectrometers, Detectors and Associated Equipment **506** (2003) 250, ISSN: 0168-9002, URL: https://www.sciencedirect.com/science/article/pii/S0168900203013688 (cit. on p. 12).

[21] M. Thomson, *Modern Particle Physics*, Cambridge University Press, 2013 (cit. on pp. 13, 14).

[22] Particle Data Group, R. L. Workman et al., *Review of Particle Physics*, PTEP **2022** (2022) 083C01 (cit. on pp. 13–15, 21).

[23] B. Povh, K. Rith, C. Scholz, F. Zetsche and W. Rodejohann, *Teilchen und Kerne: Eine Einführung in die physikalischen Konzepte*, 9th ed., Springer Spektrum, 2014, URL: https://doi.org/10.1007/978-3-642-37822-5 (cit. on p. 23).

[24]   J. W. Leachman, R. T. Jacobsen, S. G. Penoncello and E. W. Lemmon,
       Fundamental Equations of State for Parahydrogen, Normal Hydrogen, and Orthohydrogen,
       Journal of Physical and Chemical Reference Data **38** (2009) 721, ISSN: 0047-2689,
       URL: https://doi.org/10.1063/1.3160306 (cit. on p. 24).

[25]   E. Tiesinga, P. J. Mohr, D. B. Newell and B. N. Taylor,
       CODATA Recommended Values of the Fundamental Physical Constants: 2018,
       Journal of Physical and Chemical Reference Data **50** (2021) 033105, ISSN: 0047-2689,
       URL: https://doi.org/10.1063/5.0064853 (cit. on p. 24).

[26]   T. Prohaska et al., *Standard atomic weights of the elements 2021 (IUPAC Technical Report)*,
       Pure and Applied Chemistry **94** (2022) 573,
       URL: https://doi.org/10.1515/pac-2019-0603 (cit. on p. 24).

List of Figures

List of Tables